ISSN 1990-7931, Russian Journal of Physical Chemistry B, 2024, Vol. 18, No. 2, pp. 398–418. © Pleiades Publishing, Ltd., 2024.

STRUCTURE OF CHEMICAL COMPOUNDS, QUANTUM CHEMISTRY, SPECTROSCOPY

Influence of Transition Metals for Emergence of Energy Storage in Fuel Cells through Hydrogen Adsorption on the MgAl Surface

F. Mollaamin[a], *, S. Shahriari[b], and M. Monajjemi[c]

[a] *Department of Biomedical Engineering, Faculty of Engineering and Architecture, Kastamonu University, Kastamonu, Turkey*
[b] *Department of Chemistry, Central Tehran Branch, Islamic Azad University, Tehran, Iran*
[c] *Department of Chemical Engineering, Central Tehran Branch, Islamic Azad University, Tehran, Iran*
**e-mail: smollaamin@gmail.com*

Received September 23, 2023; revised November 14, 2023; accepted December 20, 2023

Abstract—In this article, the characterization of intermetallic MgAl and the possibility for hydrogen storage in the fuel cells through doping with transition metals including Ni, Pd, Pt, Cu, Ag and Au have been investigated. The importance of the electrical double layer at the interface between a metal and Mg/Al atoms together with its interaction with hydrogen molecule to produce initially electrostatic adsorption are highlighted. The important step in which molecules enable energy storage is production of a physical barrier where a physical adsorbed barrier of molecules prevent movement near the metal surface or decrease in metal reactivity where chemisorbed hydrogen molecule stick to active area on the metal surface. The projected density of state can also estimate a certain charge assembly between (Ni, Pd, Pt, Cu, Ag, Au) and MgAl surface which indicate the complex dominant of metallic features and an exact degree of covalent traits between transitions metals and MgAl surface during H_2 adsorption. In the nuclear magnetic resonance spectroscopy, it has been observed the remarkable peaks around metal elements of Ni, Pd, Pt, Cu, Ag, Au through the doping on the MgAl nanoalloy, however there are some fluctuations in the chemical shielding behaviors of isotropic and anisotropy attributes. Furthermore, all accounted $\Delta G^{o}_{\mathrm{dop}}$ amounts are very close, which demonstrate the agreement of the measured specifications by all methodologies and the reliability of the computing values.

Keywords: energy storage, fuel cell, transition metals–doped MgAl, hydrogen adsorption, CAM/LANL2DZ, density functional theory

DOI: 10.1134/S199079312402026X

INTRODUCTION

The subject of sustainable development and the application of renewable energy are crucial scales that should be taken for a shift concerning fossil fuels [1]. It has been reported intermetallic Mg_2Ni milled for ten hours by mechanical alloying and subsequently hydrogenation reports values [2, 3]. The MgH_2 system can be the most proper of all known metal hydrides that might be applied as double-faced hydrogen storage system.

Density functional theory (DFT) method was studied on the water molecule adsorption and the surface dissolution behavior of Mg alloys by adding Al, Zn, Ca, and Y atoms [4]. Generally, they found that the relative electrode potential shift of Mg–Y alloys is positive whereas that of other alloys was negative. Furthermore, the researchers used the DFT approach for calculation of Al–Cu–Mg nanoalloys, which led to stability effects during the addition of specific atom amounts in those alloys [5, 6]. Then, the properties of Li, Al, and Cd-doped Mg alloys using a first-principle calculation to calculate the cohesive energy and its electronic structure were evaluated [7]. It was also done an investigation on stepped Pt surfaces which indicated that surfaces with a lower coordination number have a higher intention to adsorb water molecules [8, 9]. It was presented an analogous adsorption manner for water clusters on both flat and stepped transition metal surfaces [10–13]. The thermodynamic behavior of dissolution in the alloy sheets of transition metals based on DFT calculations was investigated [14–21].

The authors in the previous works studied the adsorption analysis of pyridine and nitrogen heterocyclic derivatives onto pristine two-layer aluminum surface [22], pure monolayer aluminum metal surface based on Freundlich adsorption [23]. Furthermore, the data of Langmuir adsorption model of organic adsorbates containing pyridine and alkylpyridines [24]; benzotriazole, 8-hydroxyquinoline, and 2-mercaptobenzothiazole (2-MBT) [25] by using monolayer binary alloys of the Al–Mg, Al–Ga and Al–Si surfaces have been reported.

Moreover, the corrosion inhibition role of benzotriazole, 2-mercaptobenzothiazole, 8-hydroxy-

quinoline, and 3-amino-1,2,4-triazole-5-thiol on the monolayer ternary aluminum nanoalloy by addition of specific atom amounts of germanium/magnesium (Al–Mg–Ge) [26] and silicon/ magnesium (Al–Mg–Si) [27] has been estimated.

Besides, the role of pyridine and its family compounds as corrosion inhibiting agents for monolayer ternary Al nanoalloys containing Al–Mg–Si, Al–Mg–Ge, and Al–Mg–Sn surfaces have been studied [28].

In this study, a new concept of Mg–Al nanoalloy doped with transition metals of Ni, Pd, Pt, Cu, Ag, Au for adoring hydrogen molecules as an approach for energy storage in the fuel cells is proposed by using CAM-B3LYP/ LANL2DZ theoretical methods. Mg–Al alloy is relatively low in density and therefore, it is expected to extend the range of pollutants and overcome the inherit problems of poor adsorption, fast aggregation and secondary contamination in the remediation technology.

MATERIALS AND METHOD

Transition Metals-doped Mg–Al Nanoalloy and Energy Storage

The non-heat manageable alloys have the larger energy storage due to adsorption compared to the heat manageable alloys. Nevertheless, the alloys possessing the Al–Mg_2Si system also display notable energy storage process. The identical manner is seen for the alloys that do not consist of Cu in Al–Zn–Mg [29, 30].

The storing energy ability of the alloy is separate from that of the matrix will also make intergranular adsorption process. The existence of perceptible values of soluble alloying elements like Cu, Mg, Si, and Zn will cause these alloys sensitive to stress-corrosion cracking process [31, 32]. Certain elements like Cu and Mg added to Al alloys ameliorate the mechanical attributes and conduct the alloy to reply the heat dealing. The existence of magnesium also increases resistance and reduces the rate of strength loss at high temperature in the alloys.

Mg–Al alloys are lighter than other Mg-alloys and much less flammable, which can be doped with some transition metal elements including Ni, Pd, Pt, Cu, Ag, Au (Fig. 1). The great augmenting in persistence at raised temperature has been done after solution manner through activating settlement making hard due to Mg having phases.

The charge distribution of Mg–Al, Ni–MgAl, Pd–MgAl, Pt–MgAl, Cu–MgAl, Ag–MgAl, and Au–MgAl is calculated due to the Bader charge analysis [33]. The calculations have been carried out using DFT and CAM-B3LYP/LANL2DZ theoretical level [34] for measuring charge accumulation from the charge of each atom in the complex model. The changes of charge density analysis in the transition metal (TM)–doping process has illustrated that MgAl nanosurface shows the Bader charge of –9.614e, before doping and after doping the charge distribution for Ni–MgAl, Pd–MgAl, Pt–MgAl, Cu–MgAl, Ag–MgAl, and Au–MgAl have been –2.329e, –5.333e, –8.765e, –1.845e, –1.874e, and –8.636, respectively. Furthermore, the charge distribution after hydrogen molecule adsorption on the TM–doped MgAl for H_2@Ni–MgAl, H_2@Pd–MgAl, H_2@Pt–MgAl, H_2@Cu–MgAl, H_2@Ag–MgAl, and H_2@Au–MgAl have been –9.463e, –6.539e, –8.806e, –1.788e, –8.094e, and –8.625e, respectively.

Application of Density Functional theory Approach

Our computations have been carried out due to the conceptual DFT using the projector–augmented–wave methodology [34]. The Perdew–Burke–Ernzerhof functional under the generalized gradient approximation was applied as the exchange-correlation functional [35]. The nonempirical Perdew–Burke–Ernzerhof functional is recognized to relegate precise crystal specifications [36]. Commonly, where the generalized gradient approximation functionals lose out, local density functionals stop too [37].

Hohenberg–Kohn functions have rigidly made the electronic density permissible as fundamental variable to electronic and structure computations. In other words, development of the applied DFT methodology only became notable after W. Kohn and L.J. Sham released their reputable series of equations which are introduced as Kohn–Sham equations [38, 39].

Considering the electronic density within the Kohn–Sham image directs us to a remarkable reduction of the quantum computing. Thus, the Kohn–Sham methodology lightens the route for pursuing systems that cannot be discussed by conventional ab-initio methodologies. Kohn–Sham introduces the solution which brings up the mono-electronic orbitals to account the kinetic energy in a simple and relatively exact, by finding a residual modification that might be computed apart. So, one starts with a reference model of M with non-interacting electrons related to the external potential v_s and with Hamiltonian ($\hat{H}_s$) [38, 39]:

$$\hat{H}_s = -\sum_i^M \frac{1}{2}\bar{\nabla}_i^2 + \sum_i^M v_s(\vec{r}_i) = \sum_i^M \hat{h}_s,$$
$$\hat{h}_s = -\frac{1}{2}\bar{\nabla}_i^2 + v_s(\vec{r}_i), \quad (1)$$

where $\bar{\nabla}_i^2$ orbital dependent term. By representing the single particle orbitals ψ_i all electronic densities physically acceptable for the system of "non-interacting" electrons are written in the Eq. (2):

$$\rho(\vec{r}) = \sum_i^M |\psi_i(\vec{r})|^2, \quad (2)$$

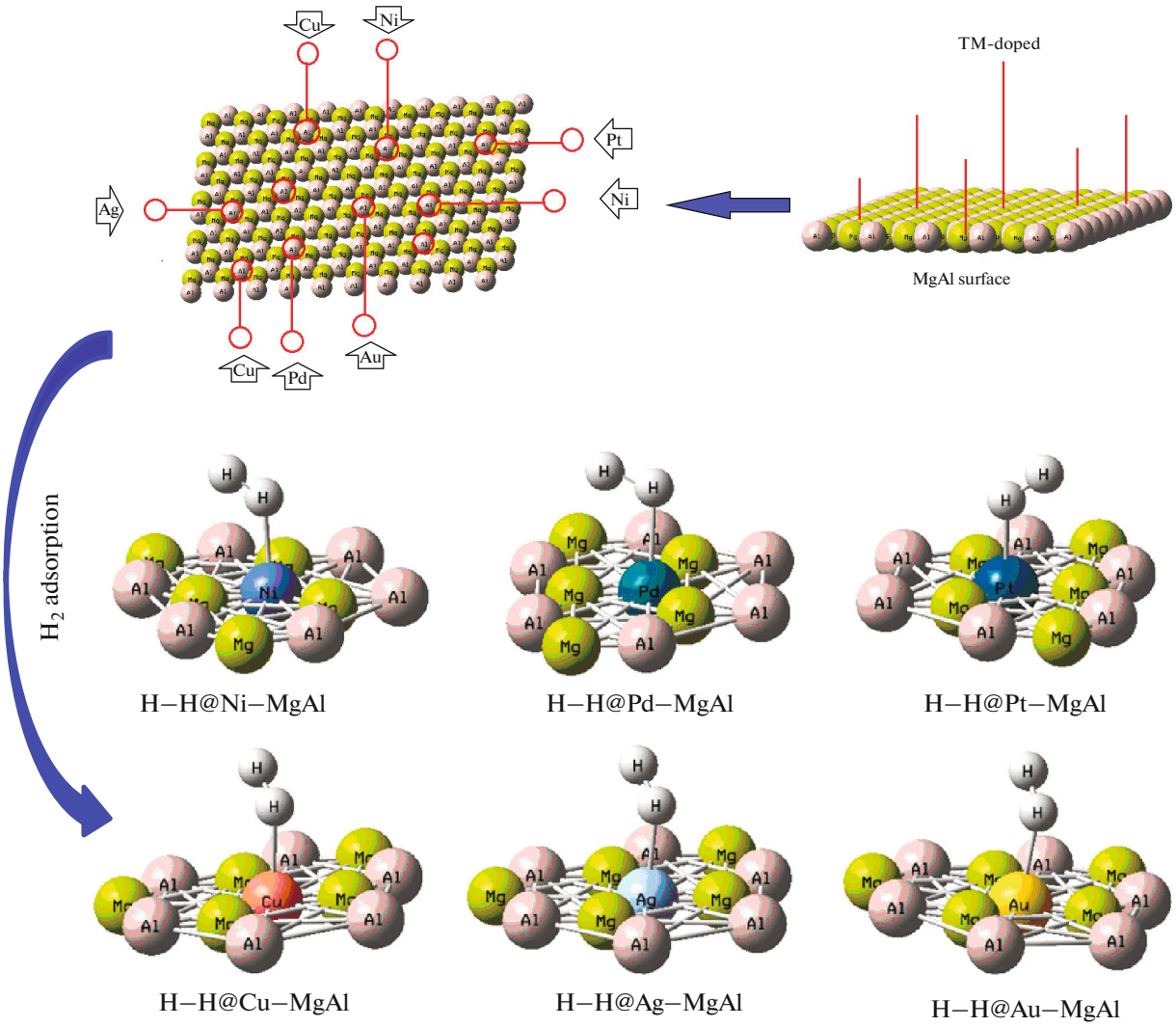

Fig. 1. The mechanism of transition metals (TM) including Ni, Pd, Pt, Cu, Ag, Au doped on the Mg–Al surface through H_2 adsorption.

where $\rho(\vec{r})$ is density and ψ_i is the corresponding Kohn–Sham orbital. Finally, the total energy $E[\rho]$ could be measured by the KS method due to the Eq. (3):

$$E[\rho] = \sum_i^M n_i \left\langle \psi_i \left| -\frac{1}{2}\bar{\nabla}^2 + v_{\text{ext}}(\vec{r}) + \frac{1}{2}\int \frac{\rho(\vec{r}')}{|\vec{r}-\vec{r}'|} d\vec{r}' \right| \psi_i \right\rangle + E_{xc}[\rho] + \frac{1}{2}\sum_{\beta}^{N}\sum_{\alpha\neq\beta}^{N} \frac{Z_\alpha Z_\beta}{|\vec{R}_\alpha - \vec{R}_\beta|}, \quad (3)$$

where v_{ext} belong to distinct Hamiltonians. Therefore, the precise exchange energy functional is described by the Kohn–Sham orbitals in lieu of the density which is cited as the indirect density functional. This research has employed the penetration of basis set of B3LYP (Becke, three-parameter, Lee–Yang–Parr) of DFT upon theoretical computations [40, 41]. The popular B3LYP and exchange-correlation functional become based on Eq. (4) [42–44]:

$$E_{xc}^{\text{B3LYP}} = (1-\alpha)E_x^{\text{LSDA}} + \alpha E_x^{\text{HF}} + b\Delta E_x^{\text{B}} + (1-c)E_c^{\text{LSDA}} + cE_c^{\text{LYP}}, \quad \alpha = 0.20,\ b = 0.72,\ c = 0.81. \quad (4)$$

E_{xc}^{B3LYP} total energy functional shows a generalized gradient approximation: the Becke exchange functional [40] and the correlation functional of Lee, Yang and Parr [41] for B3LYP and E_c^{LSDA} is the Vosko–Wilkes–Nussair local spin density approximation to the correlation functional [45].

In this article, the rigid PES using DFT calculations have been accomplished by using Gaussian 16 revision C.01 program package [46]. The input *Z*-matrix for Mg–Al nanoalloy doped with transition

metals of Ni, Pd, Pt, Cu, Ag, Au for H_2 storage in fuel cells have been provided with GaussView 6.1 [47] due to the rigid system and coordination format of which a blank line has been cited and using LANL2DZ basis set to distinguish chemical shielding, frequencies, thermodynamic properties, electrostatic and electronic potential, natural atomic charges, projected density of state and other quantum properties for this work.

RESULTS AND DISCUSSION

In this section, the physical and chemical parameters have shown the potency of MgAl nanosurface for hydrogen storage when this surface is doped with transition metals of Ni, Pd, Pt, Cu, Ag, and Au elements. In fact, it can be remarked the chemisorptive nature of the bond among the transition metals with magnesium and aluminum elements through the equilibrium distribution of transition metal elements and hydrogen molecule, and a monolayer attribute. In addition, the doped transition metals can protect the MgAl surface through binding with chemisorbed adsorbates having high protection (Fig. 1).

Density of States/projected Density of State and Electronic Evaluating

The electronic structures of (Ni, Pd, Pt, Cu, Ag, Au)-doped MgAl surface for H_2 storage in fuel cells have been investigated to simplify subsequent study for interfacial electronic properties using CAM-B3LYP/LANL2DZ basis set.

Figures 2a–2f shows the projected density of state (PDOS) of (Ni, Pd, Pt, Cu, Ag, Au)–doped MgAl surface through H_2 adsorption. The appearance of the energy states (*d*-orbital) of Ni, Pd, Pt, Cu, Ag, and Au within the gap of MgAl surface induces the reactivity of the system. It is clear from the figure that after doping with TM atoms and there is a significant contribution of TM *d*-orbital in the unoccupied level. Based on the population analysis and density of states (DOS), it can be concluded that TM remains in the cationic state, and it can accept more electrons from other atoms. Therefore, the curve of partial DOS/PDOS has described that the *p* states of the Al atoms are overcoming due to the conduction band (Figs. 2a–2f). A distinguished metallic trait might be seen in transitions metals (TMs)–MgAl nanoalloy because of the potent interaction between the *p* states of Al, and the *d* states of TM near the Fermi energy. Furthermore, the essence of covalent traits for these clusters has displayed the similar energy value and image of the PDOS for the *p* orbitals of Al and *d* orbitals of TMs including Ni, Pd, Pt, Cu, Ag, and Au through H_2 adsorption (Figs. 2a–2f).

Figures 2a–2f shows that Ni–MgAl, Pd–MgAl, Pt–MgAl, Cu–MgAl, Ag–MgAl, and Au–MgAl nanosurfaces through H_2 adsorption, respectively, have the most contribution at the middle of the conduction band between −5 to −10 eV, while contribution of aluminum and magnesium states are enlarged and similar together, and doping of nickel, palladium, platinum, copper, silver, gold increase the interfacial electronic of the MgAl nanosurface.

The partial electron density or PDOS can also estimate a certain charge assembly between (Ni, Pd, Pt, Cu, Ag, Au) and MgAl surface through H_2 adsorption. On the other hand, the above data can illustrate that the complex dominant of metallic features and an exact degree of covalent traits can describe the augmenting of the efficiency of TMs–MgAl surface for H_2 storage (Figs. 2a–2f).

Insight to Nuclear Quadrupole Resonance

In this research, the calculated nuclear quadrupole resonance/nuclear quadrupole resonance (NQR) specifications extract from electrostatic properties have been calculated for pyridine and alkylpyridines which is accord to the results of the nuclear quadrupole moment, a trait of the nucleus, and the electric field gradient/electric field gradient (EFG) in the neighborhood of the nucleus.

As the EFG at the citation of the nucleus in N-heterocycles is allocated by the valence electrons twisted in the particular attachment with close nuclei of TMs-doped MgAl nanoalloy through H_2 adsorption, the NQR frequency at which transitions occur is particular for H_2@TMs–MgAl complexes (Table 1). NQR is a straight frame of the interaction of the quadrupole moment with the EFG which is produced by the electronic structure of its ambiance. Therefore, the NQR transition frequencies are symmetric to the electric quadrupole moment of the nucleus and a measurement of the strength of the local EFG [48]. The NQR method is related to the multipole expansion in Cartesian coordinates as the Eq. (5):

$$V(r) = V(0) + \left[\left(\frac{\partial V}{\partial x_i}\right|_0 x_i\right)\Bigg] + \frac{1}{2}\left[\left(\frac{\partial^2 V}{\partial x_i x_j}\right|_0 x_i x_j\right)\Bigg] + \ldots \quad (5)$$

After that, a simplification on the equation (5), there are only the second derivatives related to the identical variable for the potential energy [48]:

$$U = -\frac{1}{2}\int_{\mathcal{D}} d^3 r \rho_r \left[\left(\frac{\partial^2 V}{\partial x_i^2}\right|_0 x_i^2\right)\Bigg] = -\frac{1}{2}\int_{\mathcal{D}} d^3 r \rho_r \times \left[\left(\frac{\partial E_i}{\partial x_i}\right|_0 x_i^2\right)\Bigg] = -\frac{1}{2}\left(\frac{\partial E_i}{\partial x_i}\right|_0 \int_{\mathcal{D}} d^3 r\left[\rho(r) x_i^2\right]. \quad (6)$$

There are two parameters which must be gotten from NQR experiments: the quadrupole coupling

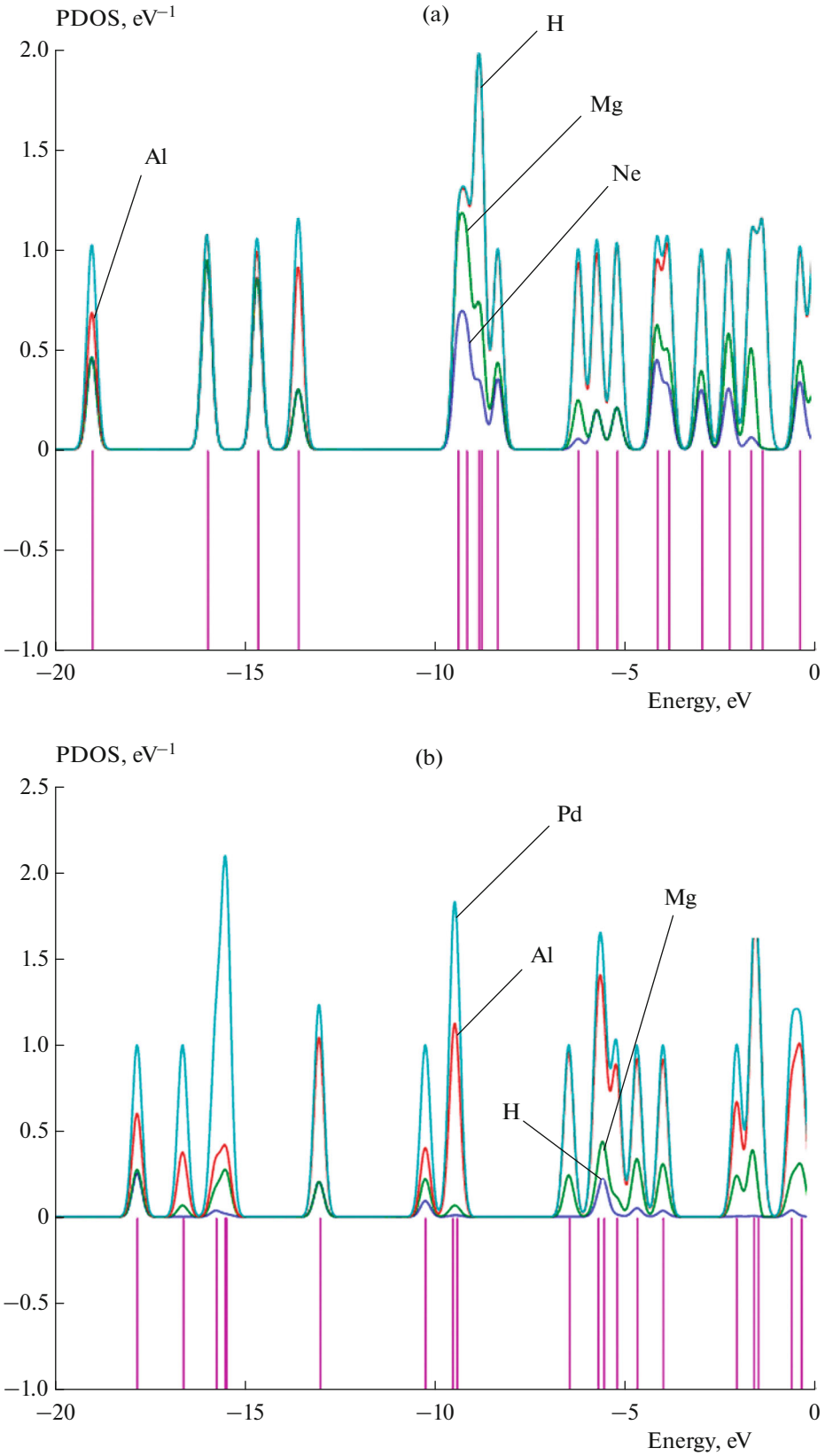

Fig. 2. Projected density of state (PDOS, eV^{-1}) versus energy (eV) of transition metals doped MgAl surface including (a) H_2@Ni–MgAl, (b) H_2@Pd–MgAl, (c) H_2@Pt–MgAl, (d) H_2@Cu–MgAl, (e) H_2@Ag–MgAl, and (f) H_2@Au–MgAl surfaces.

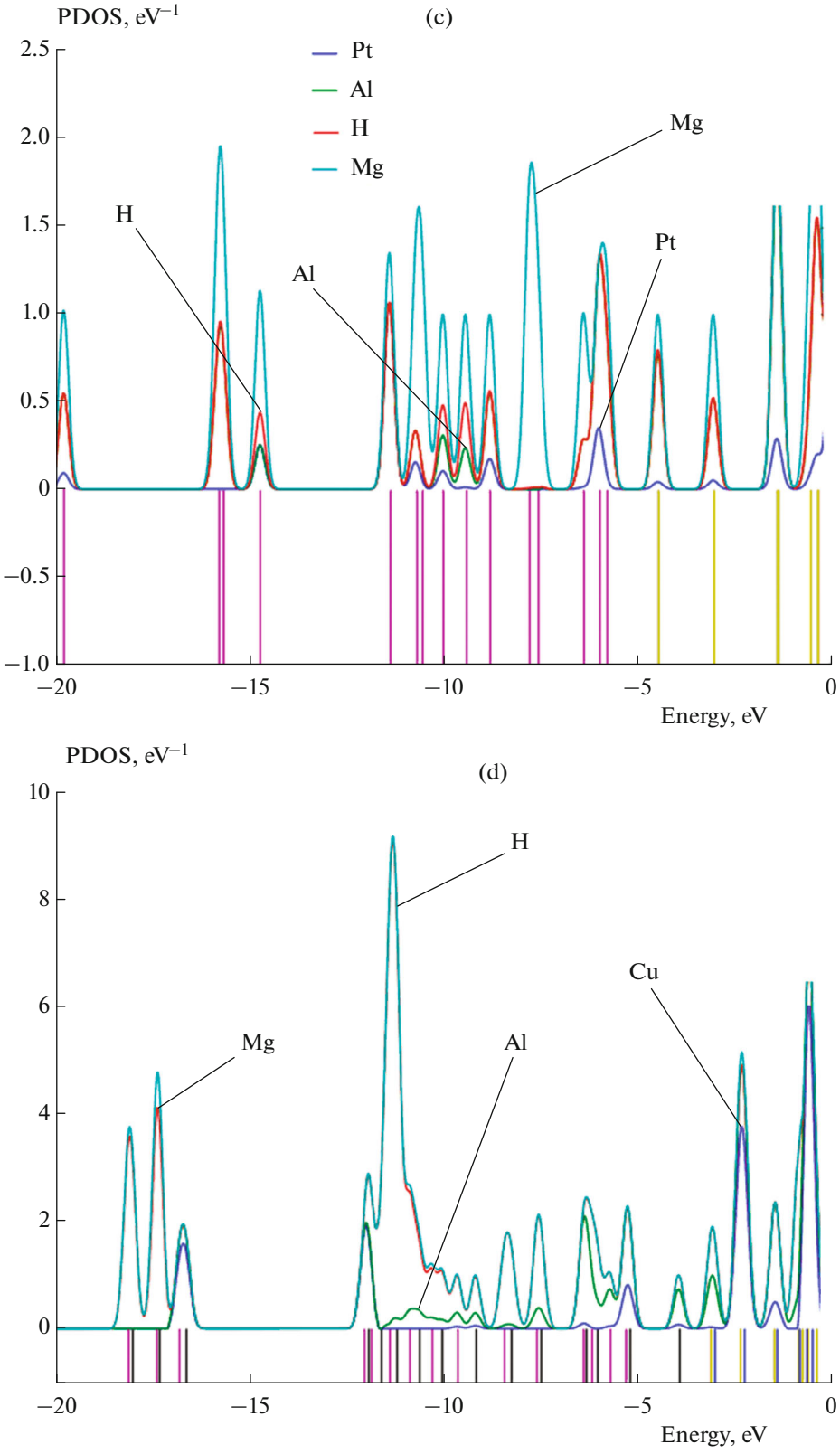
PDOS, eV^{-1}
(c)
Pt
Al
H
Mg
H
Al
Mg
Pt
2.5
2.0
1.5
1.0
0.5
0
−0.5
−1.0
−20
−15
−10
−5
0
Energy, eV
PDOS, eV^{-1}
(d)
H
Cu
Mg
Al
10
8
6
4
2
0
−20
−15
−10
−5
0
Energy, eV

Fig. 2. (Contd.)

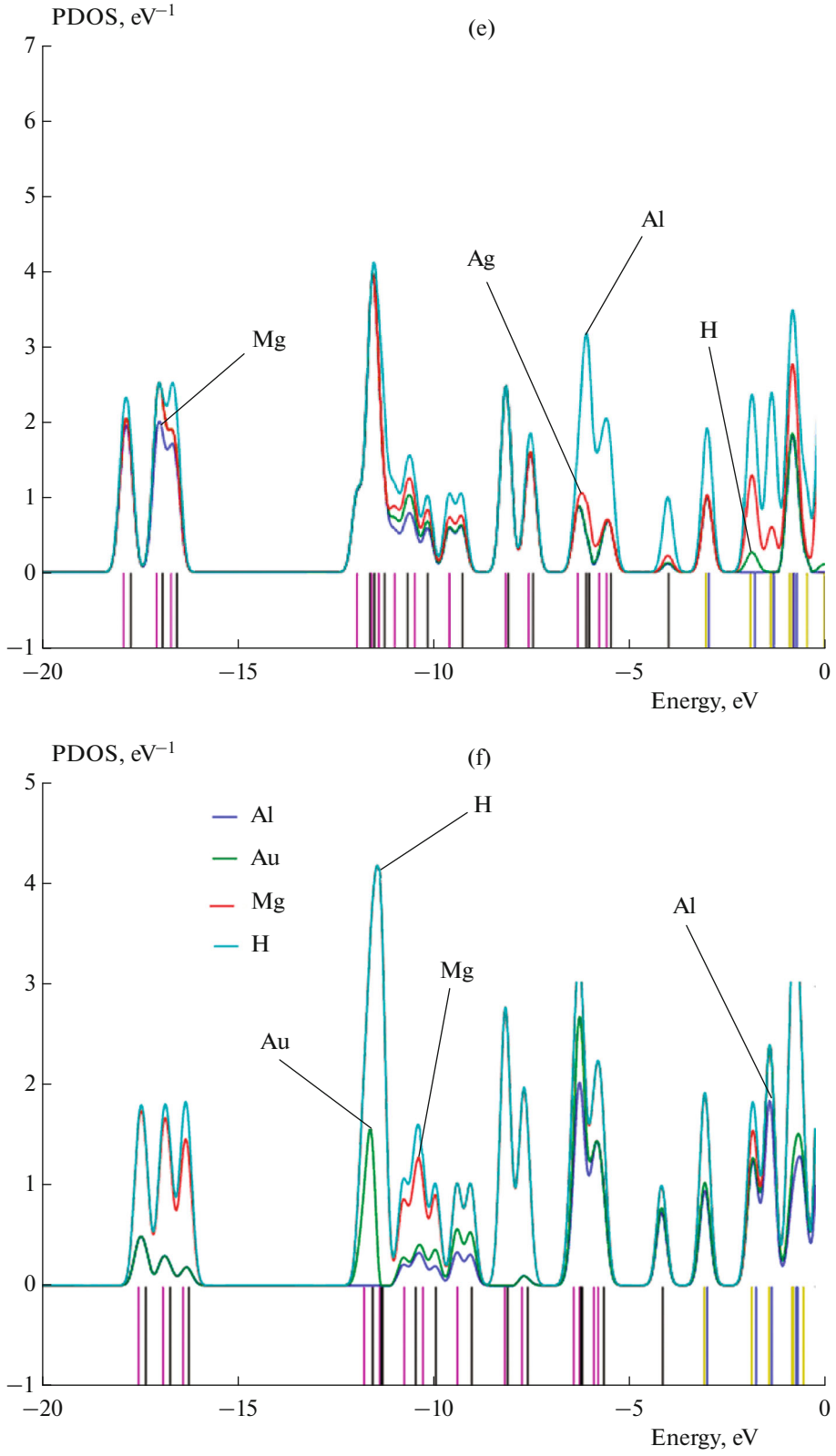
PDOS, eV^{-1}
(e)
Mg
Ag
Al
H
Energy, eV
PDOS, eV^{-1}
(f)
Al
Au
Mg
H
H
Al
Mg
Au
Energy, eV

Fig. 2. (Contd.)

Table 1. The electric potential (E_p, a.u.) and Bader charge (Q, coulomb) through NQR calculation for H_2@Ni–MgAl, H_2@Pd–MgAl, H_2@Pt–MgAl, H_2@Cu–MgAl, H_2@Ag–MgAl, and H_2@Au–MgAl surfaces using CAM-B3LYP/LANL2DZ calculation

Atom	Q	E_p	Atom	Q	E_p	Atom	Q	E_p
H_2@Ni–MgAl			H_2@Pd–MgAl			H_2@Pt–MgAl		
Al1	0.0182	−43.7382	Al1	−0.0338	−43.7456	Al1	0.7376	−0.9390
Mg2	0.8309	−38.7933	Mg2	0.9958	−38.8468	Mg2	−5.4838	0.4732
Al3	−0.3205	−43.5835	Al3	−0.3039	−43.5624	Al3	2.9293	−0.6625
Mg4	0.5156	−38.9782	Mg4	0.5072	−38.9764	Mg4	−1.2426	−0.0020
Al5	−0.0095	−43.7516	Al5	−0.0204	−43.7446	Al5	0.6791	−0.9371
Mg6	0.7916	−38.803	Mg6	0.9264	−38.8513	Mg6	−5.2867	0.4687
Ni7	−2.1888	−127.009	Pd7	−2.5927	−253.1881	Pt7	8.7102	−14.5997
Mg8	0.9043	−38.7315	Mg8	1.0971	−38.7769	Mg8	−8.3345	0.5047
Al9	−0.3977	−43.6389	Al9	−0.3997	−43.6275	Al9	2.7095	−0.6863
Al10	−0.2758	−43.5737	Al10	−0.2969	−43.5748	Al10	2.8619	−0.6728
Mg11	0.4783	−39.0013	Mg11	0.5003	−38.9858	Mg11	−1.2443	−0.0066
Al12	−0.3593	−43.6217	Al12	−0.3970	−43.6306	Al12	2.6274	−0.6882
H13	0.0078	−1.02046	H13	0.0267	−1.0934	H13	0.1210	−0.9712
H14	0.0048	−1.17693	H14	−0.0090	−1.1990	H14	0.2156	−1.0365
H_2@Cu–MgAl			H_2@Ag–MgAl			H_2@Au–MgAl		
Al1	1.6550	−0.9670	Al1	1.5199	−0.9520	Al1	0.1270	−0.9419
Mg2	−23.8952	0.2879	Mg2	−6.2106	0.4309	Mg2	0.0006	0.5277
Al3	4.5590	−0.7096	Al3	4.1463	−0.6817	Al3	0.2468	−0.6671
Mg4	0.4185	−0.0216	Mg4	−2.5051	−0.0127	Mg4	0.0287	−0.0044
Al5	1.6827	−0.9624	Al5	1.5050	−0.9538	Al5	0.0859	−0.943
Mg6	−23.1	0.2821	Mg6	−6.0237	0.4261	Mg6	0.0012	0.5219
Cu7	54.0655	−26.1309	Ag7	7.8496	−17.5414	Au7	−0.0541	−15.6039
Mg8	−29.3012	0.3196	Mg8	−10.338	0.4623	Mg8	0.2005	0.5588
Al9	4.5343	−0.6978	Al9	4.1136	−0.6982	Al9	0.0345	−0.6843
Al10	4.3849	−0.7208	Al10	4.1087	−0.6875	Al10	0.2580	−0.6742
Mg11	0.2542	−0.0226	Mg11	−2.5460	−0.0171	Mg11	−0.0002	−0.0084
Al12	4.3865	−0.7066	Al12	4.0534	−0.6975	Al12	0.0694	−0.6851
H13	0.0164	−0.9487	H13	0.0157	−0.9269	H13	0.0008	−0.9228
H14	0.3390	−0.9922	H14	0.3110	−1.0038	H14	0.0005	−1.0225

constant, χ, and asymmetry parameter of the EFG tensor η:

$$\chi = e^2 Q q_{zz}/h, \quad (7)$$

$$\eta = q_{xx} - q_{yy}/q_{zz}, \quad (8)$$

where q_{ii} are ingredients of the EFG tensor at the quadrupole nucleus determined in the EFG principal axes system, Q is the nuclear quadrupole moment, e is the proton charge and h is the Planck's constant [48].

In this research work, the electric potential as the quantity of work energy through carrying over the electric charge from one position to another position in the essence of electric field has been evaluated for H_2@Ni–MgAl, H_2@Pd–MgAl, H_2@Pt–MgAl, H_2@Cu–MgAl, H_2@Ag–MgAl, and H_2@Au–MgAl complexes using CAM-B3LYP/LANL2DZ level of theory (Table 1). Furthermore, in Figs. 3a–3f, it has been sketched the electric potential of nuclear quadrupole resonance for some atoms of aluminum, magnesium, nickel, palladium, platinum, copper, silver, and gold in the doping site on the MgAl alloy surface through H_2 adsorption which has been calculated by CAM–B3LYP/ LANL2DZ.

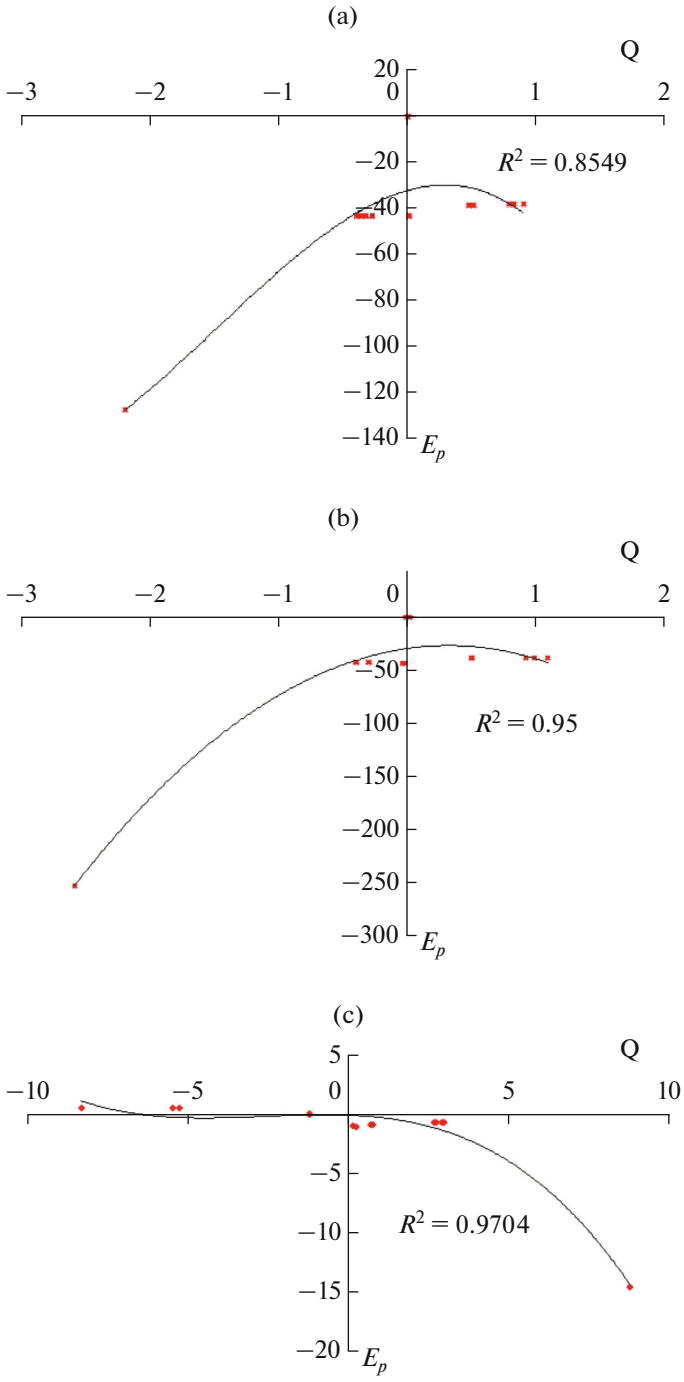

Fig. 3. The electric potential (E_p, a.u.) and Bader charge (Q, coulomb) through NQR calculation for (a) H_2@Ni–MgAl, (b) H_2@Pd–MgAl, (c) H_2@Pt–MgAl, (d) H_2@Cu–MgAl, (e) H_2@Ag–MgAl, and (f) H_2@Au–MgAl surfaces by CAM-B3LYP/LANL2DZ.

In Figs. 3a–3f, it has been described the influence of the replacement of aluminum metal elements in MgAl surface with transition metals of Ni, Pd, Pt, Cu, Ag, Au for increasing the yield of hydrogen adsorption as a model for energy storage in fuel cells. It's vivid that the curve of MgAl is waved by these transition metals. The sharpest peaks for electric potential have been shown around transition metals doping of the MgAl which presents the electron accepting characteristics of these atoms versus the aluminum and magnesium atoms of MgAl nanoalloy (Figs. 3a–3f).

Analysis of Nuclear Magnetic Resonance Spectrums

Based on resulted amounts, nuclear magnetic resonance (NMR) spectrums of TMs-doped MgAl alloy

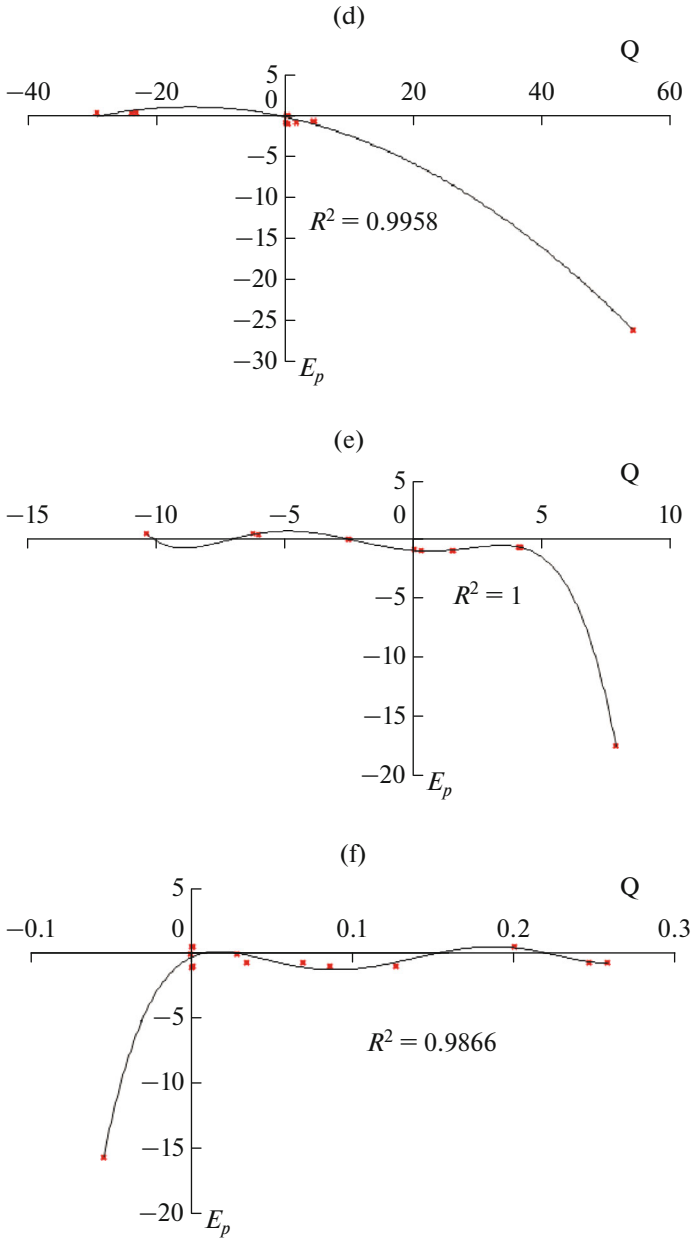

Fig. 3. (Contd.)

surface as the potent sensor for adsorbing the H_2 molecule can unravel the efficiency of transition metals containing Ni, Pd, Pt, Cu, Ag, Au in the active site of MgAl alloy surface for enhancing the value of energy storage in the fuel cells.

From the DFT calculations, it has been attained the chemical shielding tensors in the principal axes system to estimate the isotropic chemical-shielding and anisotropic chemical-shielding [49]:

$$\sigma_{iso} = \frac{\sigma_{11} + \sigma_{22} + \sigma_{33}}{3}, \quad (9)$$

$$\sigma_{aniso} = \sigma_{33} - \frac{\sigma_{22} + \sigma_{11}}{2}. \quad (10)$$

The chemical shielding extracts from NMR can be applied for allocating the structural and geometrical specifications of materials. As a matter of fact, Gauge invariant atomic orbital methodology has been recommended as a valid methodology for NMR parameter computations and Our own N-layered integrated molecular orbital and molecular mechanics has caught many regards for gaining NMR chemical shielding of gas molecule-surface complexes such as isotropic chemical shielding appears in equation (11) [50]:

$$\sigma_{iso,\ ONIOM} = \sigma_{iso,\ high(QM1)} + \sigma_{iso,medium(QM2)} + \sigma_{iso,\ low(QM3)}. \quad (11)$$

The NMR data of isotropic (σ_{iso}), anisotropic shielding tensor (σ_{aniso}) and Bader charge (Q/e) of H_2 adsorption on the transition metals doping of MgAl consisting of H_2@Ni–MgAl, H_2@Pd–MgAl, H_2@Pt–MgAl, H_2@Cu–MgAl, H_2@Ag–MgAl, and H_2@Au–MgAl surfaces have been computed by Gaussian 16 revision C.01 program package [46] and been shown in Table 2.

In Table 2, NMR data has reported the notable amounts for transition metals of Ni, Pd, Pt, Cu, Ag, Au elements which have been doped on the MgAl nanoalloy surface for H_2 adsorption.

In fact, the adsorption of hydrogen molecule can introduce spin polarization on the TM (Ni, Pd, Pt, Cu, Ag, Au)–doped MgAl nanoalloy surfaces which indicate that these surfaces might be applied as the magnetic energy storage. In fact, it is revealed that the isotropic and anisotropy shielding augment with the occupancy in the electron donating molecule adsorbed onto TM-doped MgAl nanoalloy surface. Figure 4 has exhibited the same tendency of shielding for magnesium and aluminum however a considerable deviation from transition metals of nickel (Fig. 4a),

Table 2. Data of NMR shielding tensors of isotropic (σ_{iso}, ppm) and anisotropic (σ_{aniso}, ppm) for selected atoms of H_2@Ni–MgAl, H_2@Pd–MgAl, H_2@Pt–MgAl, H_2@Cu–MgAl, H_2@Ag–MgAl, and H_2@Au–MgAl surfaces using CAM-B3LYP/LANL2DZ calculation

Atom	σ_{iso}	σ_{aniso}	Atom	σ_{iso}	σ_{aniso}	Atom	σ_{iso}	σ_{aniso}
H_2@Ni–MgAl			H_2@Pd–MgAl			H_2@Pt–MgAl		
Al1	157.7174	2474.8467	Al1	112.0096	2650.5093	Al1	164.8112	270.4088
Mg2	1320.2209	1887.0550	Mg2	307.9983	1036.5926	Mg2	134.2745	241.2676
Al3	419.6041	2091.2060	Al3	218.0989	876.5505	Al3	82.5551	113.7364
Mg4	833.8730	1992.6505	Mg4	721.4385	1036.7204	Mg4	35.5209	35.5209
Al5	196.0330	4184.2881	Al5	195.4962	3767.4506	Al5	165.2679	264.3564
Mg6	1294.4141	1612.7985	Mg6	312.7230	842.4932	Mg6	130.7628	234.7733
Ni7	1955.9386	2527.0347	Pd7	2400.9321	4326.0781	Pt7	19.3505	19.3505
Mg8	834.6838	2841.2319	Mg8	375.6286	1129.7006	Mg8	110.9214	199.2940
Al9	607.0099	2971.6196	Al9	309.7504	2277.0993	Al9	68.3011	110.8399
Al10	381.0847	2126.3884	Al10	264.6114	740.5666	Al10	78.6223	103.5533
Mg11	897.1160	897.1160	Mg11	699.5692	1175.1505	Mg11	33.4056	73.3762
Al12	503.0681	1553.4184	Al12	313.8404	1149.8812	Al12	72.6260	114.8499
H13	690.3653	2117.4887	H13	327.0050	500.6700	H13	96.1666	146.3691
H14	528.4540	1582.8654	H14	233.5832	380.1412	H14	58.8281	116.0353
H_2@Cu–MgAl			H_2@Ag–MgAl			H_2@Au–MgAl		
Al1	311.1723	1812.0387	Al1	669.8544	648.3305	Al1	7.5509	67.7485
Mg2	665.2938	440.0641	Mg2	585.5904	323.3871	Mg2	33.3593	137.8132
Al3	829.1453	586.4952	Al3	562.0512	279.4331	Al3	11.3697	64.4842
Mg4	658.9909	1697.7778	Mg4	822.5300	221.1020	Mg4	5.3316	42.0010
Al5	754.3313	1755.9199	Al5	660.1349	612.6224	Al5	4.4962	66.5346
Mg6	581.0178	341.6554	Mg6	581.1451	316.7324	Mg6	29.0226	129.2972
Cu7	2035.9544	3715.0352	Ag7	1565.6578	1033.2237	Au7	134.4877	133.9740
Mg8	582.5336	412.8669	Mg8	398.8762	208.0734	Mg8	26.9109	117.1360
Al9	881.2772	1003.4006	Al9	696.9664	415.9292	Al9	1.7706	45.8795
Al10	771.6741	993.4690	Al10	560.7053	306.0116	Al10	9.3973	59.3263
Mg11	1091.4309	1898.1756	Mg11	832.7698	272.7260	Mg11	8.2592	35.3322
Al12	659.7210	956.7105	Al12	675.1236	346.9504	Al12	3.1373	37.3247
H13	111.6583	204.8227	H13	22.0366	56.5486	H13	54.0033	96.5726
H14	74.6459	145.9247	H14	11.1420	39.6080	H14	33.5450	73.8865

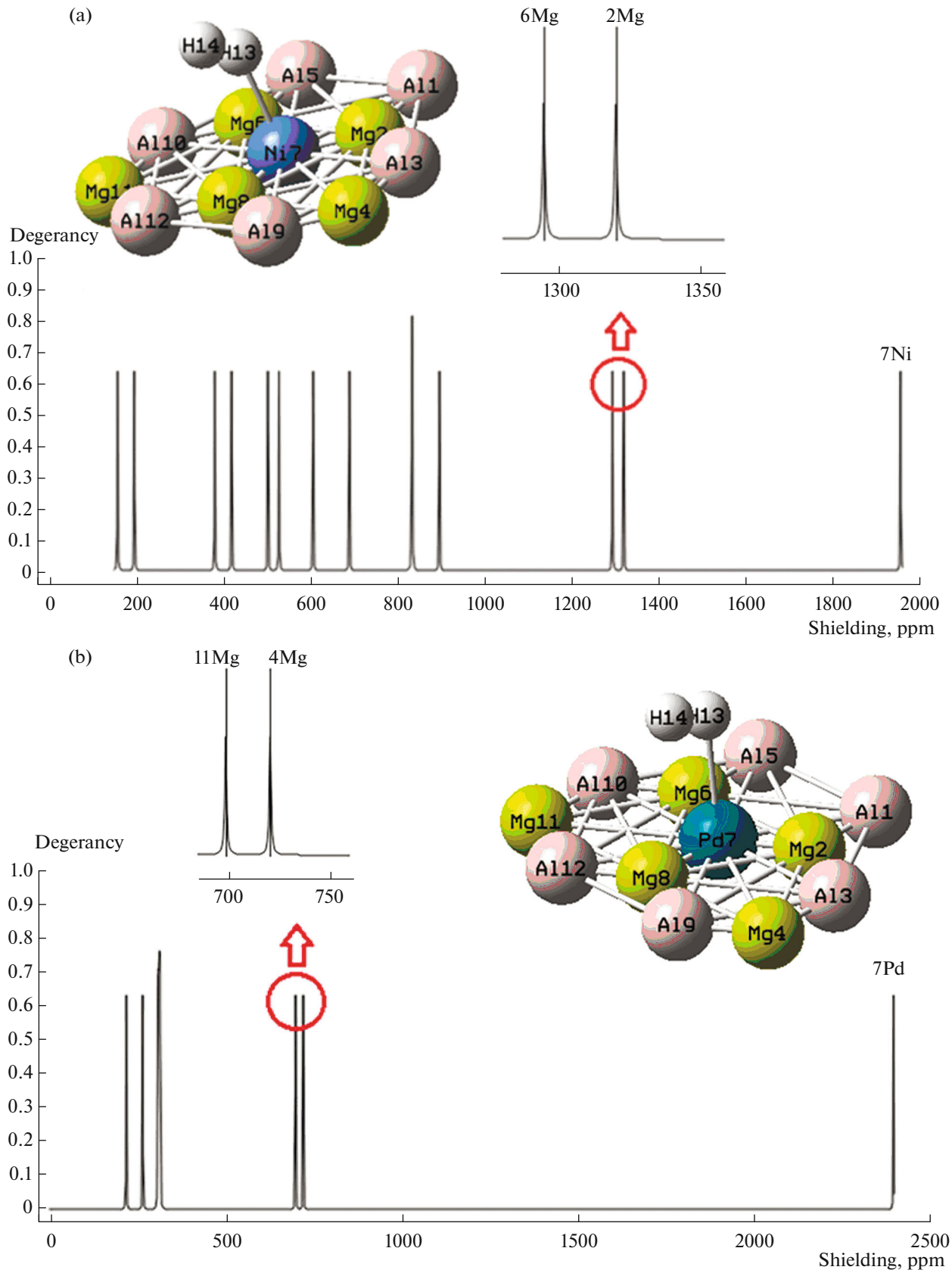

Fig. 4. The degeneracy versus shielding tensor (ppm) extracted from NMR spectrums for (a) H_2@Ni–MgAl, (b) H_2@Pd–MgAl, (c) H_2@Pt–MgAl, (d) H_2@Cu–MgAl, (e) H_2@Ag–MgAl, and (f) H_2@Au–MgAl surfaces using CAM-B3LYP/LANL2DZ.

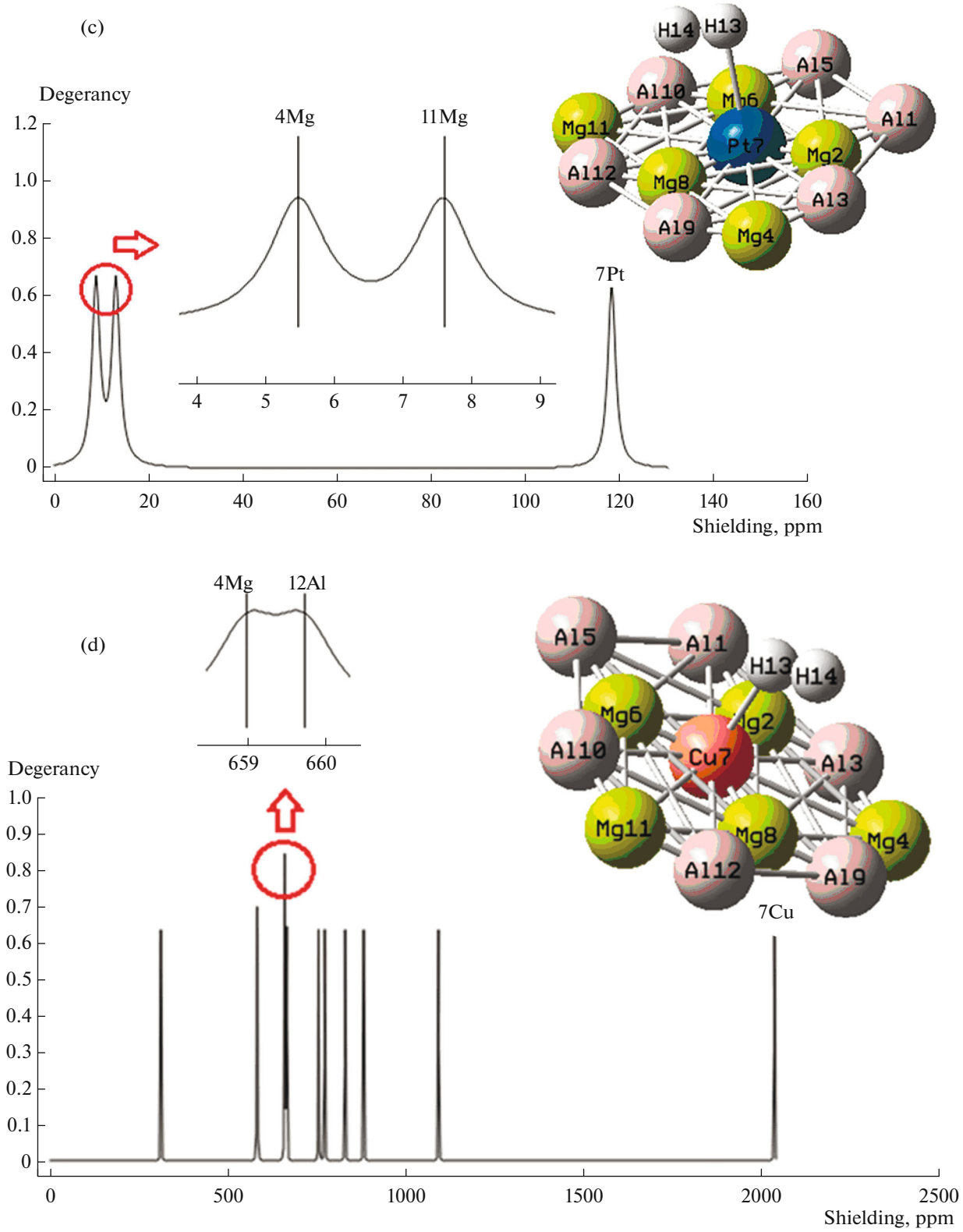
(c)
Degerancy
4Mg
11Mg
7Pt
H14
H13
A15
A110
Mg6
A11
Mg11
Pt7
Mg2
A112
Mg8
A13
A19
Mg4
Shielding, ppm
(d)
4Mg
12Al
659
660
Degerancy
A15
A11
H13
H14
Mg6
Mg2
A110
Cu7
A13
Mg11
Mg8
Mg4
A112
A19
7Cu
Shielding, ppm

Fig. 4. (Contd.)

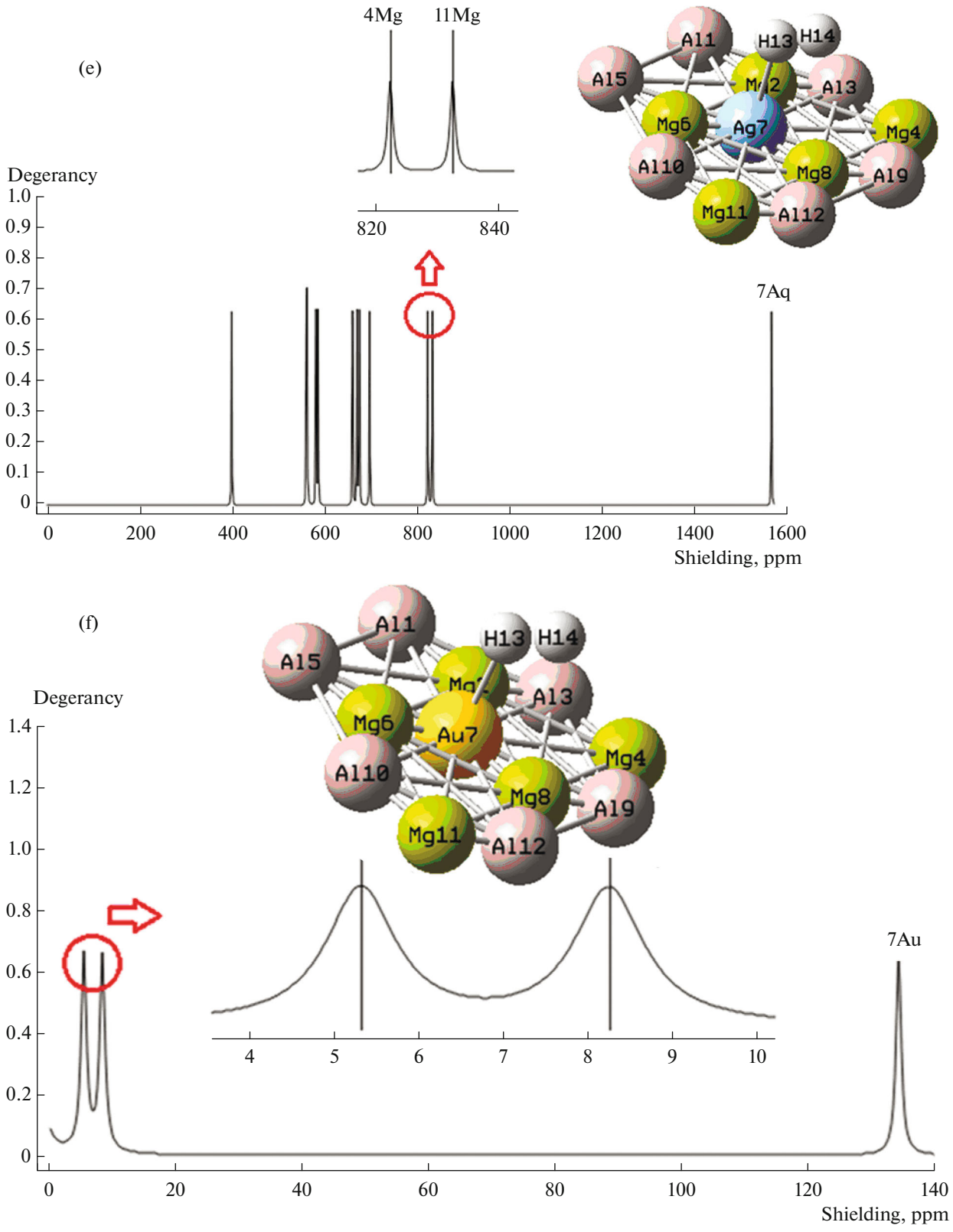
(e)
4Mg
11Mg
820
840
Al1
H13
H14
Al5
Al3
Mg6
Ag7
Mg4
Al10
Mg8
Al9
Mg11
Al12
Degerancy
1.0
0.9
0.8
0.7
0.6
0.5
0.4
0.3
0.2
0.1
0
7Aq
0
200
400
600
800
1000
1200
1400
1600
Shielding, ppm
(f)
Al1
H13
H14
Al5
Al3
Mg6
Au7
Mg4
Al10
Mg8
Al9
Mg11
Al12
Degerancy
1.4
1.2
1.0
0.8
0.6
0.4
0.2
0
4
5
6
7
8
9
10
7Au
0
20
40
60
80
100
120
140
Shielding, ppm

Fig. 4. (Contd.)

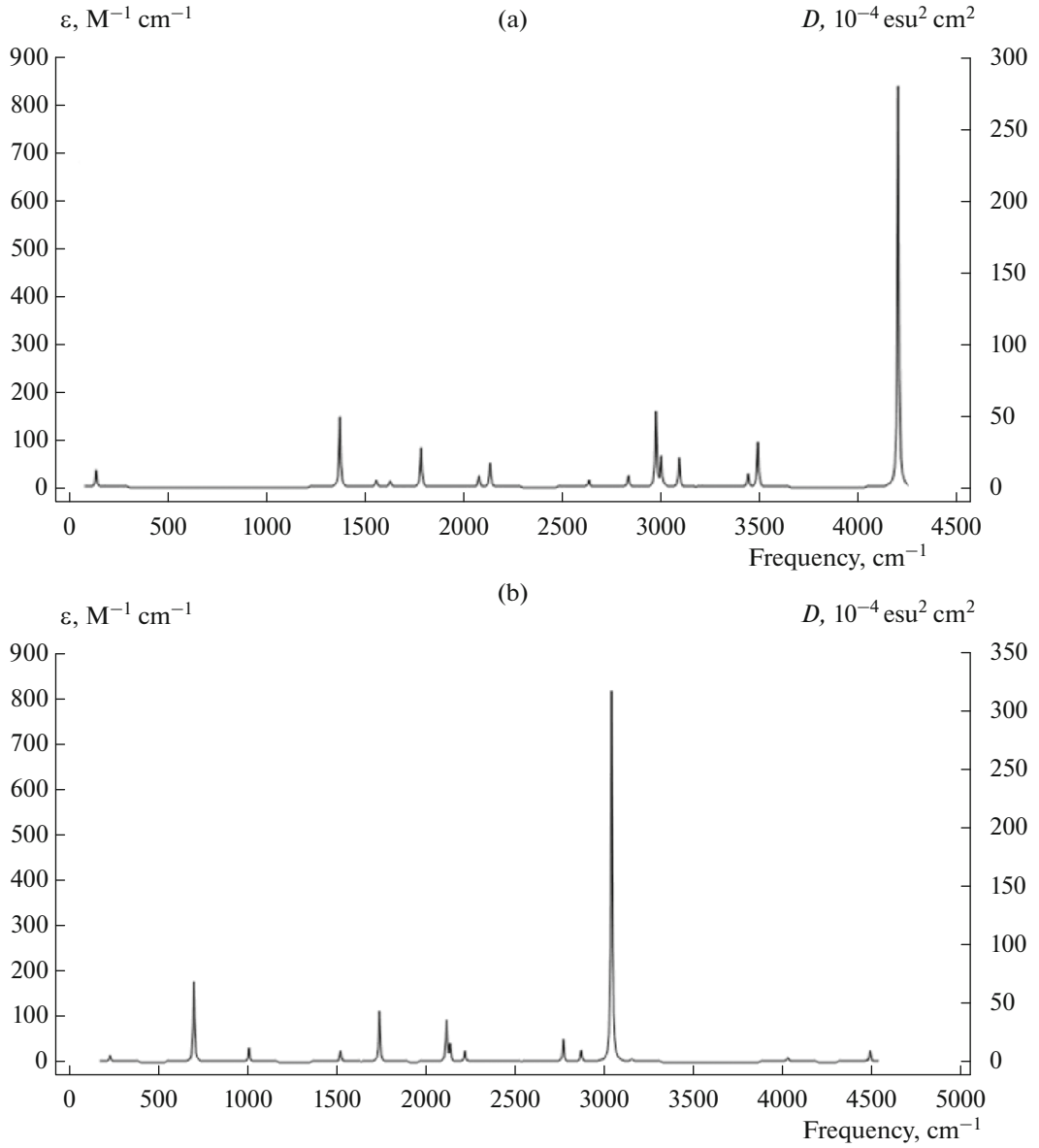

Fig. 5. The frequency (cm^{-1}) changes through the IR spectrums for (a) H_2@Ni–MgAl, (b) H_2@Pd–MgAl, (c) H_2@Pt–MgAl, (d) H_2@Cu–MgAl, (e) H_2@Ag–MgAl, and (f) H_2@Au–MgAl surfaces. ε (M^{-1} cm^{-1} or L mol^{-1} cm^{-1}) is the absorbance unit and D (10^{-4} esu^2 cm^2) is the dipole strength via the esu or electrostatic unit, which is a unit of charge in the cgs (centimeter-gram-second) system.

palladium (Fig. 4b), platinum (Fig. 4c), copper (Fig. 4d), silver (Fig. 4e), and gold (Fig. 4f) through adsorbing of hydrogen molecule.

In Figs. 4a–4f, transition metal atoms of Ni, Pd, Pt, Cu, Ag, Au in the complexes of Ni–MgAl (Fig. 4a), Pd–MgAl (Fig. 4b), Pt–MgAl (Fig. 4c), Cu–MgAl (Fig. 4d), Ag–MgAl (Fig. 4e), and Au–MgAl (Fig. 4f) denote the fluctuation in the chemical shielding during H_2 adsorption.

In fact, Figs. 4a–4f indicates that the gap chemical shielding between magnesium/aluminum in MgAl nanoalloy surface and transitions metals. Therefore, it can be considered that the efficiency of electron accepting for the transition metals doped on the MgAl nanoalloy surface is Pd > Ni ≈ Cu > Ag > Au > Pt that indicates the power of covalent bond between magnesium/aluminum and transition metal towards H_2 storage.

In the NMR spectroscopy, it has been observed the remarkable peaks around metal elements of Ni, Pd, Pt, Cu, Ag, and Au through the doping on the MgAl nanoalloy during H_2 adsorption, however there are some fluctuations in the chemical shielding behaviors of isotropic and anisotropy attributes.

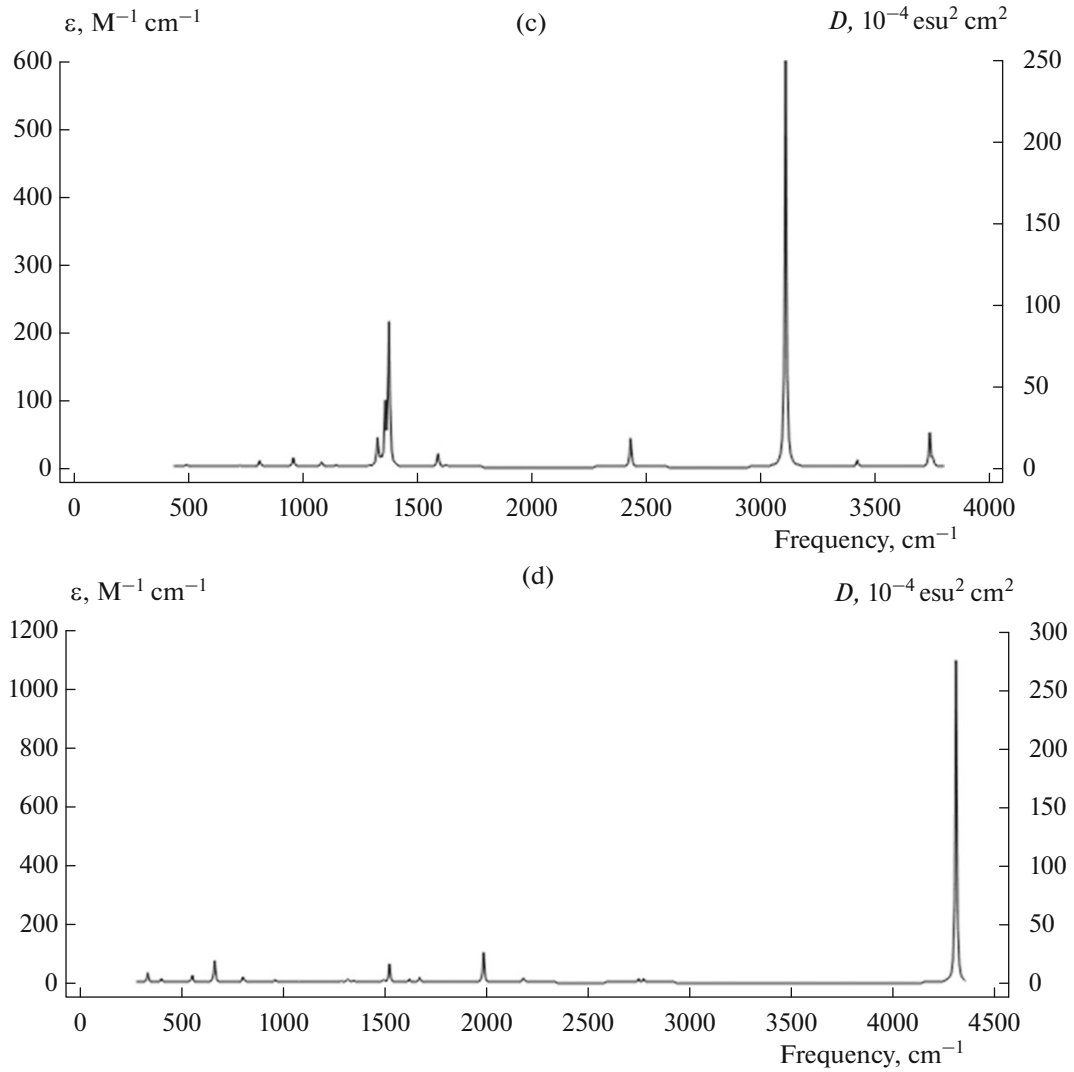

Fig. 5. (Contd.)

3.4. Infrared Spectroscopy and Thermodynamic Factors

The infrared calculations have been accomplished for doping of metal elements of Ni, Pd, Pt, Cu, Ag, Au on the MgAl nanoalloy surface during H_2 adsorption. Therefore, it has been simulated the several clusters containing H_2@Ni–MgAl (Fig. 5a), H_2@Pd–MgAl (Fig. 5b), H_2@Pt–MgAl (Fig. 5c), H_2@Cu–MgAl (Fig. 5d), H_2@Ag–MgAl (Fig. 5e), and H_2@Au–MgAl (Fig. 5f).

The graph of Fig. 4a has been observed in the frequency range between 1500–4500 cm^{-1} for H_2@Ni–MgAl nanosurface with a sharp peak around 4208.91 cm^{-1}. Figure 4b has shown the frequency range between 500–4500 cm^{-1} for H_2@Pd–MgAl nanosurface with a sharp peak around 3048.79 cm^{-1}. Figure 4c has indicated the fluctuation of frequency between 1000–4000 cm^{-1} for H_2@Pt–MgAl with several sharp peaks around 3111.16 cm^{-1}. Figure 4d has showed the fluctuation of frequency between 1000–4500 cm^{-1} for H_2@Cu–MgAl with a sharp peak around 4307.14 cm^{-1}. Moreover, it has been observed the frequency between 500–4500 for H_2@Ag–MgAl with a sharp peak around 4482.37 cm^{-1} (Fig. 4e). Besides, Fig. 4f has exhibited the frequency between 500–4500 for H_2@Au–MgAl with a sharp peak around 4542.88 cm^{-1}.

Table 3 through the thermodynamic specifications concluded that doped MgAl nanoalloy with transition metals including Ni, Pd, Pt, Cu, Ag, Au might be more efficient for adsorbing hydrogen molecules towards energy adsorption in fuel cells.

The thermodynamic data in Fig. 6 could detect the maximum efficiency of TMs–doping of MgAl nanoalloy with Ni, Pd, Pt, Cu, Ag, and Au through ΔH^o_{dop} which depends on the covalent bond between transition metals and MgAl for more and better hydrogen adsorption.

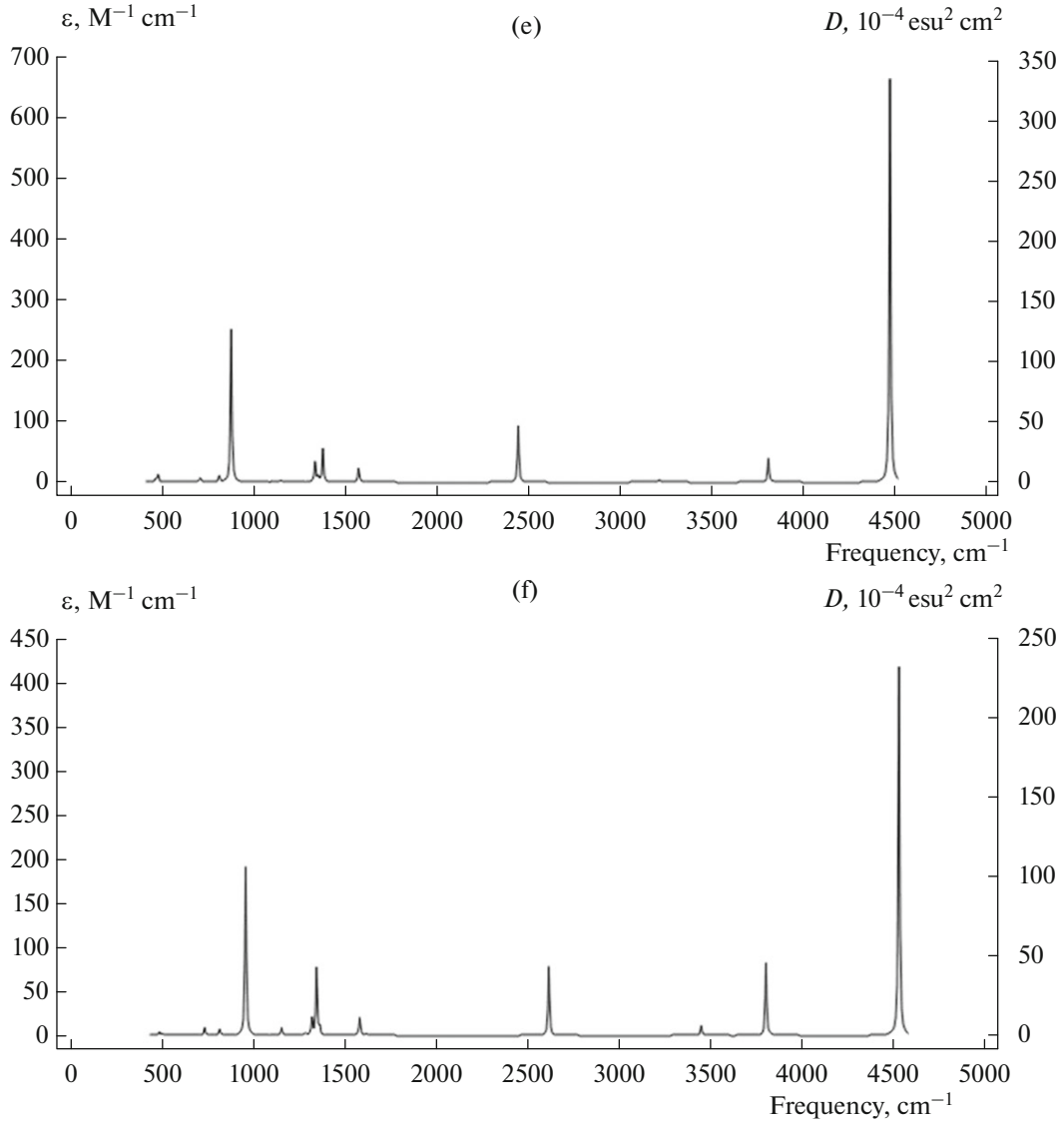

Fig. 5. (Contd.)

The doping process of transition metal on the MgAl nanoalloy surface is affirmed by the ΔH^o_{dop} quantities:

$$\Delta H^o_{\text{dop}} = \Delta H^o_{\text{X-MgAl}} - \left(\Delta H^o_{\text{X-doped}} + \Delta H^o_{\text{MgAl}}\right), \quad \text{X} = \text{Ni, Pd, Pt, Cu, Ag, Au.} \tag{12}$$

As seen in Table 3, all the accounted ΔG^o_{dop} amounts are very close, which demonstrate the agreement of the measured specifications by all methodologies and the reliability of the computing values.

Analysis of HOMO and LUMO

Based on frontier molecular orbital theory, the LUMO and HOMO and the energy between them is the band gap of the adsorption system were computed. In fact, broad band gap diagram indicates that there is less conductivity [51]. The LUMO, HOMO, and band energy gap (ΔE) of H_2 adsorption on Ni-, Pd-, Pt-, Cu-, Ag-, Au-doped MgAl nanoalloy for as the molecule detector systems denote that the molecule doping procedure scatters the electrons of the system (Table 4).

The energy gap between HOMO and LUMO has represented the transporting of molecular electrical characters [51]. On the other hand, the difference between HOMO and LUMO has exhibited the effect of (Ni, Pd, Pt, Cu, Ag, Au) doping of the MgAl nanoalloy surface on the electronic behavior of H_2@Ni–MgAl, H_2@Pd–MgAl, H_2@Pt–MgAl, H_2@Cu–MgAl, H_2@Ag–MgAl, H_2@Au–MgAl complexes (Table 4).

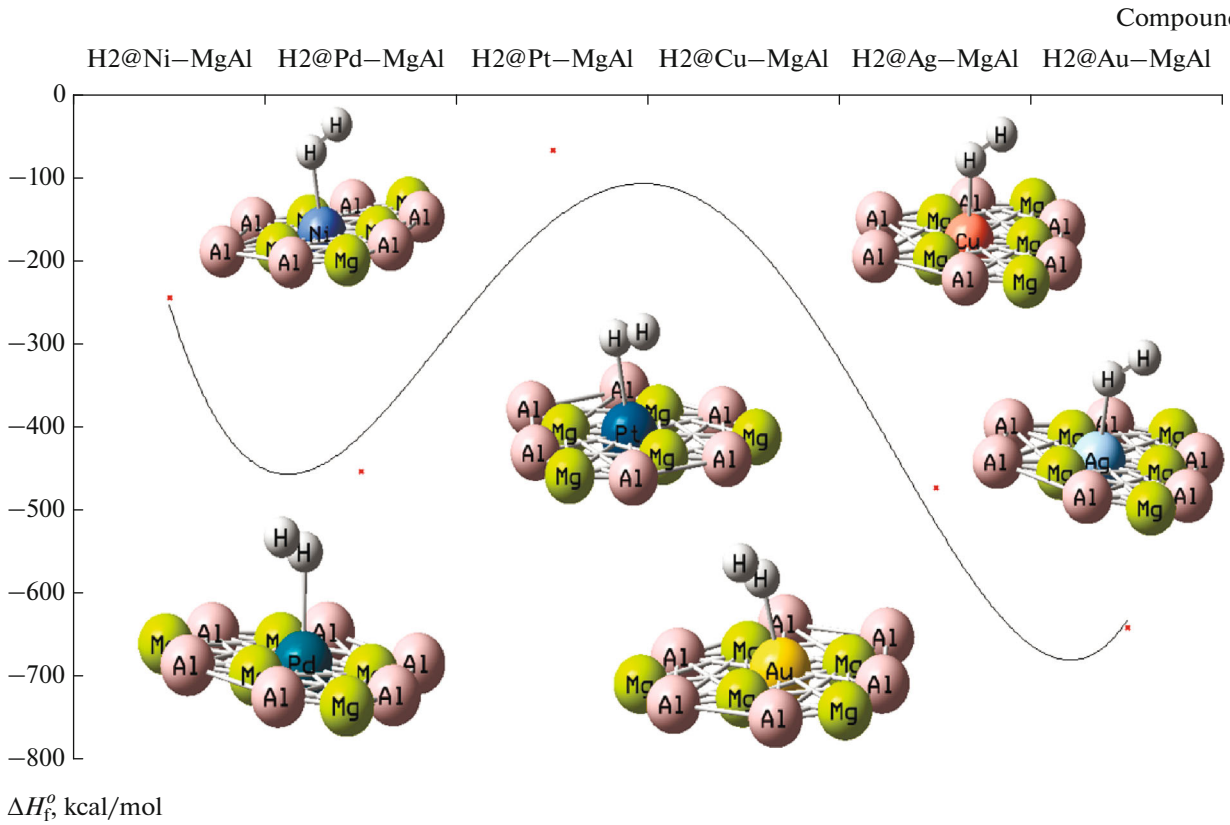

Fig. 6. Heat of formation (ΔH_f^o, kcal/mol) for H_2@Ni–MgAl, H_2@Pd–MgAl, H_2@Pt–MgAl, H_2@Cu–MgAl, H_2@Ag–MgAl, and H_2@Au–MgAl surfaces.

Table 3. The thermodynamic characters of thermal energy ($\Delta E°$, kcal/mol), thermal enthalpy ($\Delta H°$, kcal/mol), Gibbs free energy ($\Delta G°$, kcal/mol), entropy ($S°$, cal/K mol) and dipole moment (Debye)

Compound	$\Delta E° \times 10^{-4}$, kcal/mol	$\Delta H° \times 10^{-4}$, kcal/mol	$\Delta G° \times 10^{-4}$, kcal/mol	$S°$, cal/K mol	Dipole moment, Debye
H_2@Ni–MgAl	−244.8328	−244.8328	−244.8350	74.120	0.0800
H_2@Pd–MgAl	−453.9386	−453.9386	−453.9410	75.724	0.2688
H_2@Pt–MgAl	−627.3778	−67.3777	−627.3800	76.488	0.3491
H_2@Cu–MgAl	−253.0143	−253.0142	−253.0166	79.123	0.0682
H_2@Ag–MgAl	−474.1482	−474.1482	−474.1505	77.910	0.1394
H_2@Au–MgAl	−642.3836	−642.3836	−642.3971	77.810	0.4853

The illustration of donor–acceptor molecules depends on the relative frontier molecular levels. The HOMO–LUMO gap defines the charge transfer in gas molecules adsorbed on the TMs–doped MgAl surface through simplified molecular-level diagram. In fact, the amount of transferred charges might be considerably small, as in the case of parallel and perpendicular coordination, which indicate electronic couplings smaller than in co-facial coordination. The results in Table 4 have indicated the energy level shifts of H_2@TM–surface–HOMO and H_2@TM–surface–LUMO of complexes as a function of their distance *d* orbitals from the high symmetry points of each of Ni, Pd, Pt, Cu, Ag, Au doped on the MgAl nanoalloy surface.

All in all, adsorption involving charged adsorbed species causes a change in the double layer and the potential at the outer Helmholtz plane, influencing the storage rates of both anodic and cathodic reactions. The first three modes are intimately with adsorption and the double layer the last involves interaction of the hydrogen molecule and the intermediate products formed during the partial electrochemical

Table 4. LUMO (eV), HOMO (eV), and band energy gap (ΔE, eV) of H_2 adsorption on the TM–doped MgAl surface for gas storage

H_2 adsorption → TM–MgAl	HOMO	LUMO	$\Delta E = E_{LUMO} - E_{HOMO}$
H_2@Ni–MgAl	 −0.7714	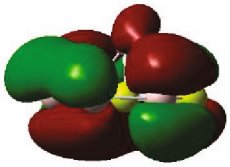 −0.0694	0.702
H_2@Pd–MgAl	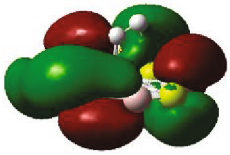 −1.0792	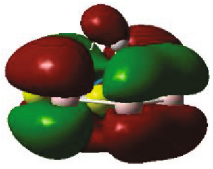 −0.3654	0.7138
H_2@Pt–MgAl	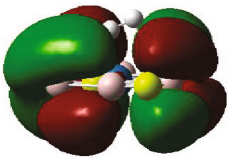 −5.7353	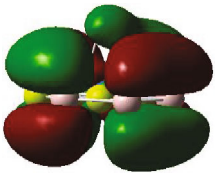 −4.4166	1.3187
H_2@Cu–MgAl	 −5.6515	 −3.0495	2.602
H_2@Ag–MgAl	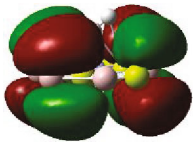 −5.8746	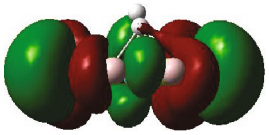 −3.0449	2.8297
H_2@Au–MgAl	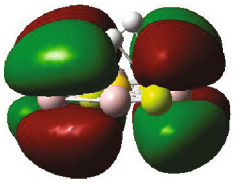 −6.9970	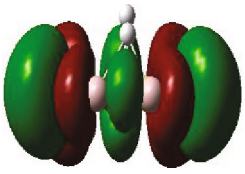 −3.5130	3.484

TM = Ni, Pd, Pt, Cu, Ag, Au.

reactions, interaction of the adsorbed intermediates with gas molecules can either decrease or increase electrode reaction rate depending on the stability of the gas molecule-intermediate complex formed.

CONCLUSIONS

This research has studied the molecular properties of hydrogen adsorption on the MgAl surface and the difference in its properties when doped with Transition metals transition metals of Ni, Pd, Pt, Cu, Ag, Au using Gaussian 16 revision C.01 program package. So, the efficiency of hydrogen storage on TMs–MgAl has been investigated through the electromagnetic and thermoelectric traits extracts from PDOS, NMR, NQR, and IR analysis which have been accomplished on H_2@Ni–MgAl, H_2@Pd–MgAl, H_2@Pt–MgAl, H_2@Cu–MgAl, H_2@Ag–MgAl, H_2@Au–MgAl complexes. In some cases, a chemical bond is formed involving charge transfer or charge sharing between the metal surface and hydrogen molecules forming a coordinate bond through lone-pair electrons on heteroatoms or π electrons on hydrogens with multiple and aromatic bonds. This article could be helpful in a range of applications which uses Mg and Mg alloy for the study of hydrogen adsorption, energy storage and its application in fuel cells. Many different approaches such as surface coatings, alloying and doping with transition metals can be adopted to make Mg and Mg alloys applicable for energy storage.

ACKNOWLEDGMENTS

In successfully completing this paper and its research, the authors are grateful to Kastamonu University.

FUNDING

This work was supported by ongoing institutional funding. No additional grants to carry out or direct this particular research were obtained.

CONFLICT OF INTEREST

The authors of this work declare that they have no conflicts of interest.

REFERENCES

1. E. Hadjixenophontos, E. M. Dematteis, N. Berti, et al., Inorganics **28**, 17 (2020). https://doi.org/10.3390/inorganics8030017
2. E. I. Rudenko, N. V. Dohlikova, A. K. Gatin, et al., Russ. J. Phys. Chem. B **17**, 845 (2023). https://doi.org/10.1134/S1990793123040164
3. S. N. Kozlov and B. E. Zhestkov, Russ. J. Phys. Chem. B **16**, 1030 (2022). https://doi.org/10.1134/S1990793122060069
4. V. Y. Agroskin, B. G. Bravy, G. K. Vasiliev, et al., Russ. J. Phys. Chem. B **16**, 596 (2022). https://doi.org/10.1134/S1990793122040029
5. F. Mollaamin and M. Monajjemi, Russ. J. Phys. Chem. **97**, 2241 (2023). https://doi.org/10.1134/S0036024423100096
6. N. V. Dokhlikova, A. K. Gatin, S. Y. Sarvadiy, et al., Russ. J. Phys. Chem. B **15**, 732 (2021). https://doi.org/10.1134/S1990793121040023
7. F. Mollaamin, M. Monajjemi, S. Salemi, et al., Fuller. Nanotub. Carbon Nanostructures **19**, 182 (2011). https://doi.org/10.1080/15363831003782932
8. N. V. Dokhlikova, S. A. Ozerin, S. V. Doronin, et al., Russ. J. Phys. Chem. B **16**, 461–467 (2022). https://doi.org/10.1134/S1990793122030137
9. M. J. Kolb, J. Wermink, F. Calle-Vallejo, L. B. Juurlink, and M. T. Koper, Phys. Chem. Chem. Phys. **18**, 3416–3422 (2016). https://doi.org/10.1039/C5CP04468E
10. A. K. Gatin, M. V. Grishin, A. S. Prostnev, et al., Russ. J. Phys. Chem. B 16, 468 (2022). https://doi.org/10.1134/S1990793122030046
11. F. Mollaamin and M. Monajjemi, J. Mol. Model. **29**, 170 (2023). https://doi.org/10.1007/s00894-023-05567-8
12. A. K. Gatin, M. V. Grishin, A. S. Prostnev, et al., Russ. J. Phys. Chem. B **16**, 468–473 (2022). https://doi.org/10.1134/S1990793122030046
13. F. Mollaamin and M. Monajjemi, J. Mol. Model. **29**, 119 (2023). https://doi.org/10.1007/s00894-023-05526-3
14. T. Würger, C. Feiler, G. B. Vonbun-Feldbauer, et al., Sci. Rep. **10**, 15006 (2020). https://doi.org/10.1038/s41598-020-71694-4
15. F. Mollaamin, A. Ilkhani, N. Sakhaei, et al., J. Comput. Theor. Nanosci. **12**, 3148–3154 (2015). https://doi.org/10.1166/jctn.2015.4092
16. M. Monajjemi, M. Khaleghian, N. Tadayonpour, et al., Int. J. Nanosci. **9**, 517–529 (2010). https://doi.org/10.1142/S0219581X10007071
17. M. Khaleghian, M. Zahmatkesh, F. Mollaamin, et al., Fuller. Nanotub. Carbon Nanostruct. **19**, 251–261 (2011). https://doi.org/10.1080/15363831003721757
18. K. Bakhshi, F. Mollaamin, and M. Monajjemi, J. Comput. Theor. Nanosci. **8**, 763–768 (2011). https://doi.org/10.1166/jctn.2011.1750
19. B. Khalili Hadad, F. Mollaamin, and M. Monajjemi, Russ. Chem. Bull. **60**, 238–241 (2011). https://doi.org/10.1007/s11172-011-0039-5
20. M. Monajjemi, F. Mollaamin, and S. Shojaei, Biointerface Res. Appl. Chem. **3**, 5575 (2020). https://doi.org/10.33263/BRIAC103.575585
21. M. A. A. Zadeh, H. Lari, L. Kharghanian, et al., J. Comput. Theor. Nanosci. 12, 4358 (2015). https://doi.org/10.1166/jctn.2015.4366
22. M. Monajjemi, F.Mollaamin, M.R. Gholami, et al., Main Group Met. Chem. 26, 349 (2003). https://doi.org/10.1515/MGMC.2003.26.6.349

23. F. Mollaamin, S. Shahriari, M. Monajjemi, et al., J. Clust. Sci. **34**, 1547–1562 (2023). https://doi.org/10.1007/s10876-022-02335-1

24. F. Mollaamin and M. Monajjemi, J. Bio. Tribo. Corros. **9**, 33 (2023). https://doi.org/10.1007/s40735-023-00751-y

25. F. Mollaamin and M. Monajjemi, Mol. Simul. **49**, 365 (2023). https://doi.org/10.1080/08927022.2022.2159996

26. F. Mollaamin and M. Monajjemi, Russ. J. Phys. Chem. B **17**, 658 (2023). https://doi.org/10.1134/S1990793123030223

27. F. Mollaamin and M. Monajjemi, Computation **11**, 108 (2023). https://doi.org/10.3390/computation11060108

28. F. Mollaamin and M. Monajjemi, J. Clust. Sci. **34**, 2901 (2023). https://doi.org/10.1007/s10876-023-02436-5

29. F. Mollaamin and M. Monajjemi, J. Mol. Struct. **1300**, 137214 (2024). https://doi.org/10.1016/j.molstruc.2023.137214

30. L. A. Wasserman, A. A. Papakhin, A. V. Krivandin, et al., Russ. J. Phys. Chem. B **16**, 141 (2022). https://doi.org/10.1134/S1990793122010328

31. V. G. Lukin, O. G. Khvostenko, L. Z. Khatymova, et al., Russ. J. Phys. Chem. B **15**, 1008 (2021). https://doi.org/10.1134/S1990793121060063

32. K. R. Kutlugildina, P. A. Chistyakova, S. A. Nikolaev, et al., Russ. J. Phys. Chem. B **15**, 399 (2021). https://doi.org/10.1134/S199079312103026X

33. G. Henkelman, A. Arnaldsson, and H. Jónsson, Comput. Mater. Sci. **36**, 354 (2006). https://doi.org/10.1016/j.commatsci.2005.04.010

34. P. E. Blöchl, Phys. Rev. B **50**, 17953 (1994). https://doi.org/10.1103/PhysRevB.50.17953

35. J. P. Perdew, K. Burke, and M. Ernzerhof, Phys. Rev. Lett. **77**, 3865 (1996). https://doi.org/10.1103/PhysRevLett.77.3865

36. P. Ziesche, S. Kurth, and J. P. Perdew, Comput. Mater. Sci. **11**, 122 (1998). https://doi.org/10.1016/S0927-0256(97)00206-1

37. M. Arrigoni and G. K. H. Madsen, Comput. Mater. Sci. **156**, 354 (2019). https://doi.org/10.1016/j.commatsci.2018.10.005

38. P. Hohenberg and W. Kohn, Inhomogeneous Electron Gas. Phys. Rev. B **136**, B864–B871 (1964). https://doi.org/10.1103/PhysRev.136.B864

39. W. Kohn and L. J. Sham, Phys. Rev. **140**, A1133–A1138 (1965). https://doi.org/10.1103/PhysRev.140.A1133

40. A. D. Becke, J. Chem. Phys. **98**, 5648 (1993). https://doi.org/10.1063/1.464913

41. C. Lee, W. Yang, R. G. Parr, Phys. Rev. B **37**, 785 (1988). https://doi.org/10.1103/PhysRevB.37.785

42. K. Kim and K. D. Jordan, J. Phys. Chem. **98**, 10089 (1994). https://doi.org/10.1021/j100091a024

43. P. J. Stephens, F. J. Devlin, C. F. Chabalowski, et al., J. Phys. Chem. **98**, 11623 (1994). https://doi.org/10.1021/j100096a001

44. C. J. Cramer, *Essentials of Computational Chemistry: Theories and Models*, 2nd ed. (Wiley, Minnesota, 2004). ISBN: 978-0-470-09182-1.

45. S. H. Vosko, L. Wilk, M. Nusair, Can. J. Phys. **58**, 1200 (1980). https://doi.org/10.1139/p80-159

46. M. J. Frisch, G. W. Trucks, H. B. Schlegel, G. E. Scuseria, M. A. Robb, J. R. Cheeseman, G. Scalmani, V. Barone, G. A. Petersson, H. Nakatsuji, X. Li, M. Caricato, A. V. Marenich, J. Bloino, B. G. Janesko, R. Gomperts, B. Mennucci, H. P. Hratchian, J. V. Ortiz, A. F. Izmaylov, J. L. Sonnenberg, D. Williams-Young, F. Ding, F. Lipparini, F. Egidi, J. Goings, B. Peng, A. Petrone, T. Henderson, D. Ranasinghe, V. G. Zakrzewski, J. Gao, N. Rega, G. Zheng, W. Liang, M. Hada, M. Ehara, K. Toyota, R. Fukuda, J. Hasegawa, M. Ishida, T. Nakajima, Y. Honda, O. Kitao, H. Nakai, T. Vreven, K. Throssell, J. A. Montgomery, Jr., J. E. Peralta, F. Ogliaro, M. J. Bearpark, J. J. Heyd, E. N. Brothers, K. N. Kudin, V. N. Staroverov, T. A. Keith, R. Kobayashi, J. Normand, K. Raghavachari, A. P. Rendell, J. C. Burant, S. S. Iyengar, J. Tomasi, M. Cossi, J. M. Millam, M. Klene, C. Adamo, R. Cammi, J. W. Ochterski, R. L. Martin, K. Morokuma, O. Farkas, J. B. Foresman, and D. J. Fox, *Gaussian 16, Revision C.01* (Gaussian, Inc., Wallingford CT, 2016).

47. R. Dennington, T. A. Keith, and J. M. Millam, *GaussView, Version 6.06.16* (Semichem Inc., Shawnee Mission, KS, 2016). https://gaussian.com/gaussview6/. Accessed on February 11, 2023.

48. M. L. Jabbar and K. J. Kadhim, Russ. J. Phys. Chem. B **15**, 46–52 (2021). https://doi.org/10.1134/S1990793121010188

49. A. A. Lundin and V. E. Zobov, Russ. J. Phys. Chem. B **15**, 839 (2021). https://doi.org/10.1134/S1990793121050079

50. V. F. Kablov, V. L. Strakhov, V. O. Kaledin, et al., Russ. J. Phys. Chem. B **15**, 880 (2021). https://doi.org/10.1134/S1990793121050043

51. F. Akman, Russ. J. Phys. Chem. B **15**, 517 (2021). https://doi.org/10.1134/S1990793121030027